

correspond to the eigenmodes of the Schmidt decomposition of the biphoton wave function created in the 4WM process. This type of theoretical analysis was carried out for PDC (33). A measure of the spatial entanglement is provided by the Schmidt number, which is the “average” number of Schmidt modes involved. A rough estimate of that number is given by the number of gain-medium diffraction-limited Gaussian twin beams that fit into the solid angle of acceptance (23), and it naturally matches the previous estimate of the number of independent modes, counted in terms of non-overlapping coherence areas (25, 34). Such a large Schmidt number highlights the potential of this system as a source of high-dimensional entanglement. The exact details of the entanglement, contained in the coefficients of the Schmidt decomposition, depend on the spatial gain profile and can be tuned by varying the spatial mode of the pump laser. A major challenge will be to use that degree of freedom to generate and detect useful multimode states.

References and Notes

- M. I. Kolobov, Ed., *Quantum Imaging* (Springer, New York, 2007).
- M. I. Kolobov, C. Fabre, *Phys. Rev. Lett.* **85**, 3789 (2000).

- A. Mosset, F. Devaux, E. Lantz, *Phys. Rev. Lett.* **94**, 223603 (2005).
- N. Treps et al., *Science* **301**, 940 (2003).
- S. L. Braunstein, P. van Loock, *Rev. Mod. Phys.* **77**, 513 (2005).
- M. D. Reid, P. D. Drummond, *Phys. Rev. Lett.* **60**, 2731 (1988).
- L.-M. Duan, G. Giedke, J. I. Cirac, P. Zoller, *Phys. Rev. Lett.* **84**, 2722 (2000).
- R. Simon, *Phys. Rev. Lett.* **84**, 2726 (2000).
- Z. Y. Ou, S. F. Pereira, H. J. Kimble, K. C. Peng, *Phys. Rev. Lett.* **68**, 3663 (1992).
- J. Laurat, T. Coudreau, G. Keller, N. Treps, C. Fabre, *Phys. Rev. A* **70**, 042315 (2004).
- A. S. Villar, L. S. Cruz, K. N. Cassemiro, M. Martinelli, P. Nussenzveig, *Phys. Rev. Lett.* **95**, 243603 (2005).
- J. Jing, S. Feng, R. Bloomer, O. Pfister, *Phys. Rev. A* **74**, 041804 (2006).
- C. Silberhorn et al., *Phys. Rev. Lett.* **86**, 4267 (2001).
- H. Yonezawa, S. L. Braunstein, A. Furusawa, *Phys. Rev. Lett.* **99**, 110503 (2007).
- P. Kumar, M. I. Kolobov, *Opt. Commun.* **104**, 374 (1994).
- A. Mair, A. Vaziri, G. Weihs, A. Zeilinger, *Nature* **412**, 313 (2001).
- J. C. Howell, R. S. Bennink, S. J. Bentley, R. W. Boyd, *Phys. Rev. Lett.* **92**, 210403 (2004).
- L. Lopez, N. Treps, B. Chalopin, C. Fabre, A. Maître, *Phys. Rev. Lett.* **100**, 013604 (2008).
- M. Lassen et al., *Phys. Rev. Lett.* **98**, 083602 (2007).
- C. F. McCormick, V. Boyer, E. Arimondo, P. D. Lett, *Opt. Lett.* **32**, 178 (2007).
- P. R. Hemmer et al., *Opt. Lett.* **20**, 982 (1995).
- M. D. Lukin, P. R. Hemmer, M. O. Scully, *Adv. At. Mol. Opt. Phys.* **42**, 347 (2000).
- Materials and methods are available as supporting material on *Science* Online.
- C. F. McCormick, A. M. Marino, V. Boyer, P. D. Lett, preprint available at <http://arxiv.org/abs/quant-ph/0703111> (2007).
- V. Boyer, A. M. Marino, P. D. Lett, *Phys. Rev. Lett.* **100**, 143601 (2008).
- All uncertainties quoted in this paper represent 1 SD, combined statistical and systematic uncertainties.
- M. I. Kolobov, *Rev. Mod. Phys.* **71**, 1539 (1999).
- P. Navez, E. Brambilla, A. Gatti, L. A. Lugiato, *Phys. Rev. A* **65**, 013813 (2001).
- M. D. Reid, *Phys. Rev. A* **40**, 913 (1989).
- C. Kim, P. Kumar, *Phys. Rev. Lett.* **73**, 1605 (1994).
- V. Delaubert et al., *Phys. Rev. A* **74**, 053823 (2006).
- M. T. L. Hsu, W. P. Bowen, N. Treps, P. K. Lam, *Phys. Rev. A* **72**, 013802 (2005).
- C. K. Law, J. H. Eberly, *Phys. Rev. Lett.* **92**, 127903 (2004).
- O. Jedrkiewicz et al., *Phys. Rev. Lett.* **93**, 243601 (2004).
- R.C.P. is supported under a grant from the Intelligence Community Postdoctoral Program.

Supporting Online Material

www.sciencemag.org/cgi/content/full/1158275/DC1

Materials and Methods

SOM Text

Figs. S1 and S2

References

25 March 2008; accepted 4 June 2008

Published online 12 June 2008;

10.1126/science.1158275

Include this information when citing this paper.

Phase Transitions of Dirac Electrons in Bismuth

Lu Li,^{1*} J. G. Checkelsky,¹ Y. S. Hor,² C. Uher,³ A. F. Hebard,⁴ R. J. Cava,² N. P. Ong^{1*}

The Dirac Hamiltonian, which successfully describes relativistic fermions, applies equally well to electrons in solids with linear energy dispersion, for example, in bismuth and graphene. A characteristic of these materials is that a magnetic field less than 10 tesla suffices to force the Dirac electrons into the lowest Landau level, with resultant strong enhancement of the Coulomb interaction energy. Moreover, the Dirac electrons usually come with multiple flavors or valley degeneracy. These ingredients favor transitions to a collective state with novel quantum properties in large field. By using torque magnetometry, we have investigated the magnetization of bismuth to fields of 31 tesla. We report the observation of sharp field-induced phase transitions into a state with striking magnetic anisotropy, consistent with the breaking of the threefold valley degeneracy.

The Dirac Hamiltonian, long the accepted theory of relativistic fermions, is equally successful in describing electrons in solids, notably bismuth (1–3), Bi_{1–x}Sb_x (4), and graphene (5, 6). Unlike in regular solids, the electron energy, $E(\mathbf{p})$, in these materials is linear in the momentum, \mathbf{p} , just as in relativistic

fermions. However, Dirac electrons living in solids have two distinguishing features. First, because of their small (or zero) mass gap, the Dirac bands become quantized into Landau levels in a modest magnetic field, \mathbf{H} . A striking consequence in graphene is the observation of the integer quantum Hall effect (QHE) (5, 6). The Coulomb interaction energy is crucially important when all electrons are confined to the lowest Landau level. Secondly, the Dirac electrons in solids come in different “flavors,” corresponding to orbital valley degeneracy. The interplay of strong interaction and degeneracy suggests that, in intense \mathbf{H} , a phase transition may occur to a collective state

with novel quantum properties (7). In bismuth, the Dirac electrons occupy three Fermi surface (FS) ellipsoids. By using a torque cantilever to measure its magnetization, we have observed sharp field-induced transitions. The high-field ordered state is magnetically anisotropic, consistent with the breaking of the flavor (valley) degeneracy.

In bismuth, the hole FS ellipsoid is aligned with the trigonal axis \mathbf{z} (8) (Fig. 1A, inset). The three-electron FS ellipsoids, arrayed symmetrically around the hole FS, are tilted by a small angle β ($\sim 6.5^\circ$) out of the plane defined by the bisectrix (\mathbf{x}) and binary (\mathbf{y}) axes. Extensive studies have established that the electron ellipsoids have a Dirac dispersion (1, 2, 9, 10). In the geometry with $\mathbf{H} \parallel \mathbf{z}$, each Landau level of the electrons has a threefold valley degeneracy. However, the near-equality of the hole and electron FS areas (projected onto the xy plane) has long stymied efforts to resolve the quantum oscillations of the electrons from the holes (11–14). This roadblock has to be overcome before the Dirac electrons can be investigated. We solved this problem with torque magnetometry (8) [section I of supporting online material (SOM)]. Two sets of data were taken to maximum $H=14$ T and to 31 T (at temperatures of 1.5 and 0.3 mK, respectively) on single crystals in which the resistance ratio (between 300 K and 4 K) RRR is ~ 100 .

In an increasing \mathbf{H} , the Landau level energies rise. As each sublevel crosses the chemical potential μ and empties, a break-in-

¹Department of Physics, Princeton University, NJ 08544, USA. ²Department of Chemistry, Princeton University, NJ 08544, USA. ³Department of Physics, University of Michigan, Ann Arbor, MI 48109, USA. ⁴Department of Physics, University of Florida, Gainesville, FL 32611, USA.

*To whom correspondence should be addressed. E-mail: luli@princeton.edu (L.L.); npo@princeton.edu (N.P.O.)

slope appears in the free energy F versus H (eq. S5 of SOM). We assume \mathbf{H} is at an angle θ to a FS symmetry axis $\hat{\mathbf{e}}$. In terms of the area $S(\theta)$ of the FS section normal to \mathbf{H} , the breaks occur at the fields $B_n(\theta)$ given by

$$\frac{1}{B_n} = \frac{2\pi e}{\hbar} [n + \gamma] \frac{1}{S(\theta)}, \quad (n = 0, 1, 2, \dots) \quad (1)$$

where e is the electron charge, $2\pi\hbar$ is Planck's constant, and γ the Onsager phase. We label the sublevels as (n, s) , where $s = \pm 1$ indexes the Kramers doublet.

In the tilted \mathbf{H} , a torque, $\boldsymbol{\tau}$, appears with magnitude given by $\tau = -\partial F/\partial\theta$. The torque arises because the orbital, diamagnetic moment \mathbf{m} tends to align with $\hat{\mathbf{e}}$ if $\theta \ll 1$. Hence, the Landau eve crossings may be observed as a series of sharp anomalies in a trace of τ versus H (fig. S1). In addition to the high-field oscillations, the torque also senses a featureless "background" term $\Delta\chi_b$ arising from the unusually large diamagnetic susceptibility (3).

The symmetry between the three ellipsoids is broken by tilting \mathbf{H} in the yz plane (Fig. 1A inset). Because the cantilever by design responds to the x component of $\boldsymbol{\tau}$ only, it is sensitive to the torques from ellipsoids 2 and 3 and less so to the holes from ellipsoid 1 and nearly invisible; see eq. S16 of SOM).

We expressed the torque signal τ as a transverse magnetization, viz. $M_T = \tau/VH$, with V the sample volume. In Fig. 1, curves of M_T versus H are displayed with θ confined to the narrow window $(-4^\circ, 4^\circ)$ in which the transitions occur. As shown, $M_T(H)$ contains a dense set of quantum oscillations, which mostly arise from the electron FS. At large H , we observed sharp, hysteretic jumps at a field H_2 that shifts rapidly with θ . As θ increases from -3.5° to -0.3° (Fig. 1A), the transition field H_2 (black arrows) increases from 14 to 24 T. For $\theta > 0$ (Fig. 1B), H_2 falls back to 13 T as $H_2 \rightarrow 2.1^\circ$. In addition, a transition occurs at the lower field H_1 (red arrows).

First, we identified the electron quantum oscillations by using the derivatives $\partial M_T/\partial H$ in the low-field set. Figure 2, A and B, shows curves measured at $\theta = -3.1^\circ$ and 3.4° , respectively. As indicated, the index fields $B_{n,s}$ appear as sharp minima for $\theta < 0$ and as sharp maxima for $\theta > 0$ (fig. S3). When displayed in the $\theta - H$ plane, the index fields $B_{n,s}$ describe a nominally symmetric pattern (Fig. 2C). The set of 19 angles investigated and the smooth variations versus θ allow us to sort out most of the sublevels. By Eq. 1, the θ dependence of $B_{n,s}$ reflects the angular dependence of S in ellipsoids 2 and 3. Fields $B_{n,s}$ that increase with increasing θ arise from 2, and those that decrease with increasing θ arise from 3. At large H , the sign of τ provides further guidance. When a sublevel (n, s) crosses the symmetry line $\theta = 0$, its contribution to τ changes sign. The changes

$(1, -) \rightarrow (1', -)$ and $(2, \pm) \rightarrow (2', \pm)$ are indicated in Fig. 2, A and B (the high-field partner is primed).

A plot of $1/B_{n,\pm}$ versus the integers n (at a fixed θ) gives a straight line with a slope corresponding to an electron FS area $S_e = 6.21$ T (fig. S6). The large number of oscillations ($n = 0, \dots, 10$) allows a test of the Dirac spectrum (1-3) compared with the conventional spectrum. Our measurements agree well with the former but are incompatible with the latter in the limit $n \rightarrow 0$ (section IV of SOM). Hence, the Dirac spectrum underlies the sublevel indexing shown in Figs. 2 and 3.

In Fig. 2C, the lower transition field $H_1(\theta)$ stands out because its dispersion is anomalous (open circles). In contrast to the indexed sublevels, $H_1(\theta)$ displays a hull-shaped bottom with sides rising steeply as $|\theta| \rightarrow 4^\circ$ (fig. S5). Remarkably, within the region shaded white, the curve of the sublevel $(0, -)$, which intersects H_1 , loses its intensity abruptly, as discussed below.

Extending the analysis to 31 T, we can map out the high-field phase diagram. In Fig. 3, the white area is now apparent as a cone-

shaped region bounded by H_1 from below and by H_2 from above (black curves). As $|\theta| \rightarrow 4^\circ$, the two curves meet at the field ~ 13 T. From Fig. 1A we see that, in curves with $\theta > 0$, M_T displays a step downward (red arrow) as we enter this region, followed by a step upward (black arrow) as we exit. The sublevel $(0, -)$ line vanishes on entering this region (fig. S5). At angles $|\theta| > 4^\circ$, it reappears outside the cone region, rising to 17.5 T at $\theta = 11^\circ$ (blue circles). Within the cone region, the electronic state is distinct from that outside.

This difference is apparent if we make H -constant cuts of the transverse magnetization $M_T(\theta, H)$ versus θ . Figure 4A shows curves at several H values increasing from 10 to 31 T in 1-T steps (curves are displaced by 10 A/m for clarity). All the curves display a "background" term that is θ -linear with a nominally H -independent slope. By its sign, we may identify it with the anisotropy $\Delta\chi_b = \chi_x - \chi_y$ of the unusually large diamagnetic susceptibility (3).

At the lower field values (10 to 14 T), M_T exhibits jumps when θ crosses the curve of H_1 (shown as red circles). These are the jumps indicated by the red arrows in Fig. 1. As H rises

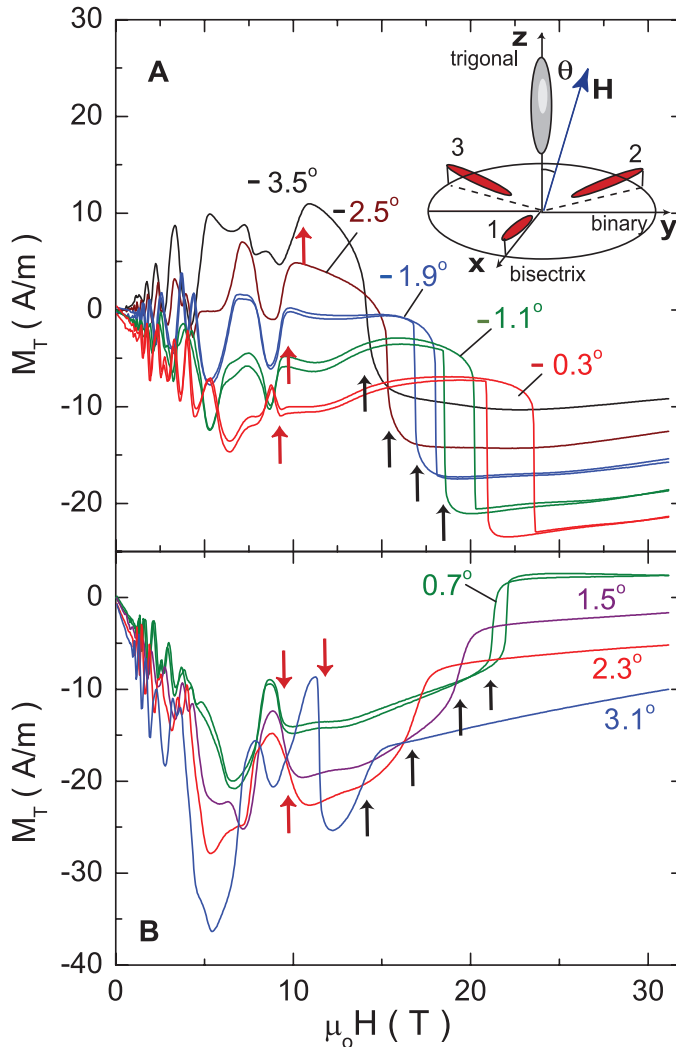


Fig. 1. The H dependence of the torque signal displayed as $M_T = \tau/VH$, with \mathbf{H} at angles $|\theta| < 4^\circ$. (A) and (B) show curves with $\theta < 0$ and $\theta > 0$, respectively. In each curve, electronic transitions are observed at H_1 (red arrows) and at H_2 (black arrows). [(A) inset] The hole (gray) and electron (red) FS ellipsoids. \mathbf{H} lies in the yz plane. The sign of M_T is that of $\boldsymbol{\tau} \cdot \mathbf{x}$. μ_0 is the vacuum permeability.

Fig. 2. Traces of the derivative dM_T/dH versus $H = |\mathbf{H}|$ at $\theta = -3.1^\circ$ and 3.4° [(A) and (B), respectively] at 1.5 K. The sublevels (n, s) are identified by minima for $\theta < 0$, and sublevels ($s = \pm$) are identified by maxima for $\theta > 0$. Primed labels, for example, ($2', +$), indicate sublevels that have crossed the line $\theta = 0$. At low H , the label ($n, +$) is shortened to n . (C) The dispersion of sublevels (n, s) versus θ in the θ - H plane with H in log scale. As θ increases, sublevels with $B_{n,s}$ decreasing belong to ellipsoid 2, and sublevels with $B_{n,s}$ increasing belong to ellipsoid 3. At large H , the sublevels ($1, \pm$) and ($2, \pm$) may be followed over a broad range of θ . The hole sublevel $n = 1$ is the θ -independent curve at 9.2 T (triangles). The curve H_1 (open circles) is the lower boundary of a new state.

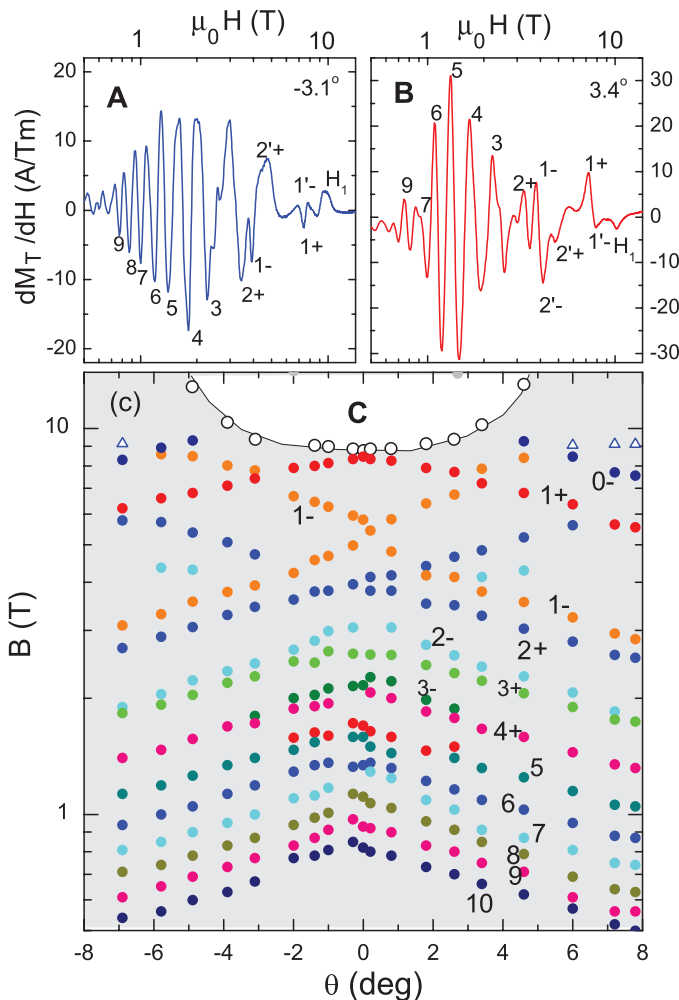
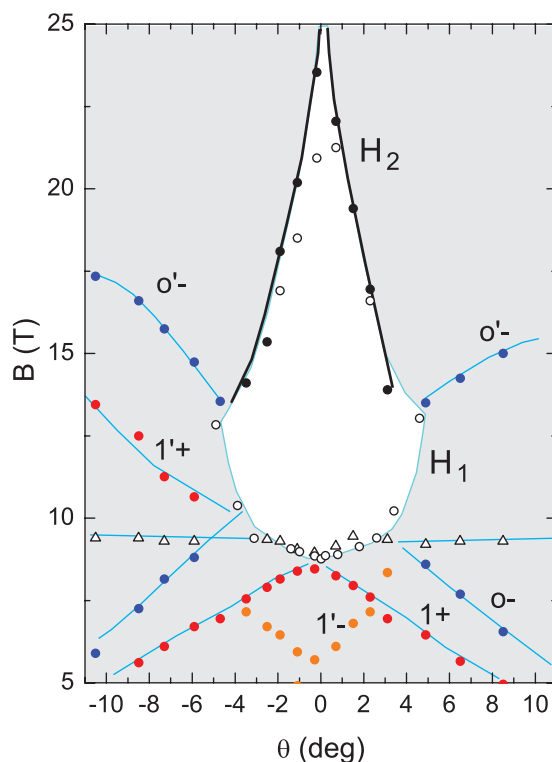


Fig. 3. High-field phase diagram in the B - θ plane ($T = 0.3$ K). The two transition fields H_2 (red circles) and H_1 (open circles) enclose a region (white) in which the torque signal vanishes (apart from the background $\Delta\chi_b$). The sublevel ($0, -$) vanishes in amplitude when it enters this region but reappears at larger tilt $|\theta|$. The horizontal line at 9.3 T is the $n = 1$ sublevel of the hole ellipsoid.



to values 14 to 25 T, the jumps occur when θ crosses H_2 (black circles). With increasing H , the interval bounded by the curve $H_2(\theta)$ steadily shrinks, until it falls below our angular spacing $\delta\theta \sim 1^\circ$ above 25 T.

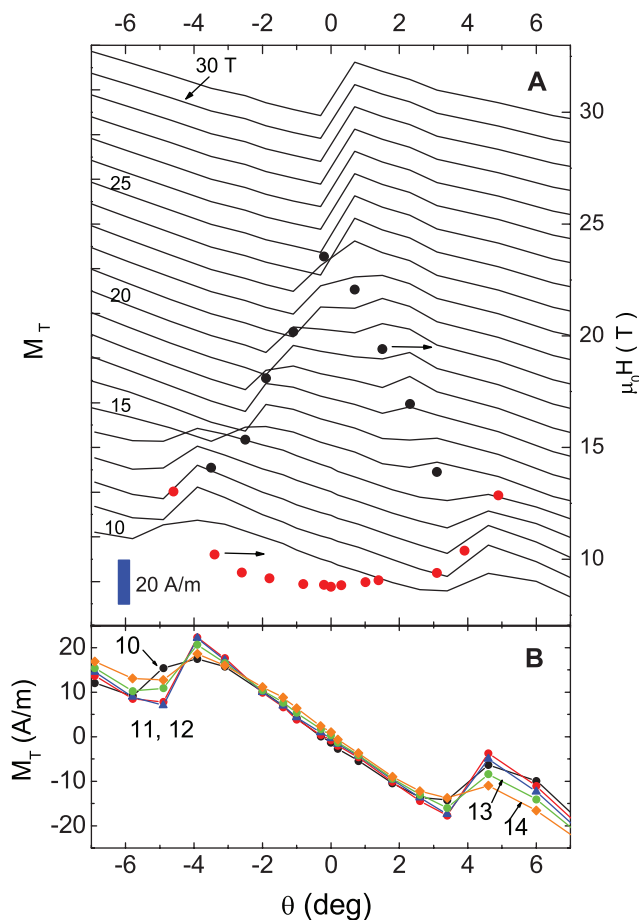
A striking feature is the uniform topography of $M_T(\theta, H)$ throughout the cone region. This is emphasized in Fig. 4B, which replots the low-field curves without displacing them. Within the cone, $M_T(\theta, H)$ stays independent of H despite a 40% increase in H . Identifying the common slope of M_T versus θ with the background term $\Delta\chi_b$, we infer that there is no further contribution to the torque in the quantum limit; the high-field torque is clamped at zero inside the cone region. This accounts for the vanishing of the signal from $(0, -)$ as its trajectory enters the cone region. When we leave this region, by changing either H or θ , a finite high-field torque reappears as a jump discontinuity at the boundaries H_1 and H_2 . The first-order nature of the jumps and the finite angular width of the cone region suggest that, as H is tilted slightly from \mathbf{z} , the system persists in the zero-torque state. The steep decrease of $H_2(\theta)$ with increasing $|\theta|$ also emphasizes the importance of the threefold degeneracy to the zero-torque state. A slight tilt of \mathbf{H} allows the state to be destabilized at a lower H_2 .

The state above the curve of $H_2(\theta)$ is also unexpected (Fig. 4A). In constant- H cuts at large H , $M_T(\theta)$ undergoes a finite jump at $\theta = 0$, abruptly reaching a nominally constant value on both sides. Ignoring the background slope, we may express the profile as $M_T = \text{sgn}(\theta)M_0$, with M_0 independent of θ and \mathbf{H} . This profile implies saturation of the transverse magnetization, as well as an abrupt sign change at $\theta = 0$. If viewed as a plot of M_T versus H_y , it is suggestive of a ferromagnetic response (but not involving the physical spins). By contrast, M_T at $n = 0$ for noninteracting electrons does not saturate (see eq. S13 of SOM). Both the saturation and sign change imply that the noninteracting Landau level scheme is inadequate in high fields.

The problem of interacting electrons with several valley degrees is also of importance in the 2D (two-dimensional) QHE systems based on bilayer GaAs (7, 15, 16) and graphene (17–19). In the large- H limit, the electrons gain exchange energy if they all occupy the same valley (or a linear combination of valleys). This state, involving “valley polarization,” is called valley ferromagnetism. In bismuth (with $\mathbf{H} \parallel \mathbf{z}$), the presence of a threefold valley degeneracy enriches the problem in a novel way; the system may either form a symmetric combination of the three valleys or occupy two of them. The magnetic anisotropy and ferromagnetic-like profile revealed in Fig. 4 strongly suggest a valley-polarized state.

Our results confirm that, in bismuth, the Dirac electrons with three flavors are unstable to the formation of a novel ground state in intense mag-

Fig. 4. Constant-field cuts of the transverse magnetization $M_T(\theta, H)$. **(A)** Cuts for $10 < H < 31$ T in 1-T steps, displaced by 10 A/m between adjacent curves (blue bar indicates $\Delta M_T = 20$ A/m). Transitions occur when θ crosses the curves H_1 (red circles) and H_2 (black circles). The background tilt arises from the susceptibility anisotropy $\Delta\chi_{cb}$. At high fields ($H > 25$ T), M_T retains its discontinuity at $\theta = 0$. **(B)** Cuts at 10 to 14 T without displacement. In the angular window $|\theta| < 4^\circ$, M_T is independent of H .



netic fields. The 3D electronic state in bismuth is easier to probe with thermodynamic and spectroscopic tools and hence promising for elucidating the high-field instability of the Dirac gas.

Reference and Notes

1. M. H. Cohen, E. I. Blount, *Philos. Mag.* **5**, 115 (1960).
2. P. A. Wolff, *J. Phys. Chem. Solids* **25**, 1057 (1964).
3. H. Fukuyama, R. Kubo, *J. Phys. Soc. Jpn.* **28**, 570 (1970).

4. D. Hsieh *et al.*, *Nature* **452**, 970 (2008).
5. K. S. Novoselov *et al.*, *Nature* **438**, 197 (2005).
6. Y. Zhang, Y.-W. Tan, H. L. Stormer, P. Kim, *Nature* **438**, 201 (2005).
7. K. Moon *et al.*, *Phys. Rev. B* **51**, 5138 (1995).
8. D. Shoenberg, *Magnetic Oscillations in Metals* (Cambridge Univ. Press, Cambridge, 1984).
9. R. N. Brown, J. G. Mavroides, B. Lax, *Phys. Rev.* **129**, 2055 (1963).
10. M. Maltz, M. S. Dresselhaus, *Phys. Rev. B* **2**, 2877 (1970).
11. R. N. Bhargava, *Phys. Rev.* **156**, 785 (1967).
12. F. Y. Yang *et al.*, *Phys. Rev. B* **61**, 6631 (2000).
13. S. G. Bompadre, C. Biagini, D. Maslov, A. F. Hebard, *Phys. Rev. B* **64**, 073103 (2001).
14. K. Behnia, L. Balicas, Y. Kopelevich, *Science* **317**, 1729 (2007).
15. S. Q. Murphy, J. P. Eisenstein, G. S. Boebinger, L. N. Pfeiffer, K. W. West, *Phys. Rev. Lett.* **72**, 728 (1994).
16. Y. P. Shkolnikov, S. Misra, N. C. Bishop, E. P. De Poortere, M. Shayegan, *Phys. Rev. Lett.* **95**, 066809 (2005).
17. K. Nomura, A. H. MacDonald, *Phys. Rev. Lett.* **96**, 256602 (2006).
18. J. Alicea, M. P. A. Fisher, *Phys. Rev. B* **74**, 075422 (2006).
19. J. G. Checkelsky, L. Li, N. P. Ong, *Phys. Rev. Lett.* **100**, 206801 (2008).
20. We thank B. A. Bernevig, M. Z. Hasan, and D. A. Huse for useful comments and S. Hannahs and T. Murphy for valuable help. This research is supported by NSF (grant no. DMR 0213706). High-field measurements were carried out in the National High Magnetic Field Laboratory, Tallahassee, which is supported by NSF cooperative agreement no. DMR-0084173, by the state of Florida, and by the U.S. Department of Energy.

Supporting Online Material

www.sciencemag.org/cgi/content/full/321/5888/547/DC1
Materials and Methods
SOM Text
Figs. S1 to S6
References

9 April 2008; accepted 9 June 2008
10.1126/science.1158908

Did Cooling Oceans Trigger Ordovician Biodiversification? Evidence from Conodont Thermometry

Julie A. Trotter,^{1,2*} Ian S. Williams,¹ Christopher R. Barnes,³ Christophe Lécuyer,⁴ Robert S. Nicoll⁵

The Ordovician Period, long considered a supergreenhouse state, saw one of the greatest radiations of life in Earth's history. Previous temperature estimates of up to $\sim 70^\circ\text{C}$ have spawned controversial speculation that the oxygen isotopic composition of seawater must have evolved over geological time. We present a very different global climate record determined by ion microprobe oxygen isotope analyses of Early Ordovician–Silurian conodonts. This record shows a steady cooling trend through the Early Ordovician reaching modern equatorial temperatures that were sustained throughout the Middle and Late Ordovician. This favorable climate regime implies not only that the oxygen isotopic composition of Ordovician seawater was similar to that of today, but also that climate played an overarching role in promoting the unprecedented increases in biodiversity that characterized this period.

Oxygen isotopes provide a valuable means for tracking environmental change, with oxygen isotopic compositions of marine fossil carbonates ($\delta^{18}\text{O}_{\text{carb}}$) being especially use-

ful for reconstructing Cenozoic sea-surface temperatures (T). This approach, however, has proven less reliable for older biogenic carbonates, which are more prone to diagenetic modification. Anom-

alously low oxygen isotope compositions of Early Paleozoic biogenic carbonates have driven contentious debate about the implied high seawater temperatures and variability in seawater oxygen isotopic composition ($\delta^{18}\text{O}_{\text{seawater}}$). Resolution of these issues has important implications for understanding fundamental Earth processes and major events in Earth history.

The Paleozoic marine $\delta^{18}\text{O}_{\text{carb}}$ record is derived mainly from calcitic brachiopods (2, 3) that exhibit a wide range in composition from about -2 per mil (‰) to -10 ‰ Vienna Pee Dee bellemnite (V-PDB). It has been argued that this re-

¹Research School of Earth Sciences, The Australian National University, Mills Road, Canberra ACT 0200, Australia. ²CSIRO Petroleum Resources, North Ryde, NSW 1670, Australia. ³School of Earth and Ocean Sciences, University of Victoria, Victoria, BC V8W 2Y2, Canada. ⁴Laboratoire CNRS UMR 5125 Paléoenvironnements et Paléobiosphère, Université Claude Bernard Lyon 1, Campus de la Doua, F-69622 Villeurbanne, France. ⁵Department of Earth and Marine Sciences, Australian National University, Canberra ACT 0200, Australia.

*To whom correspondence should be addressed. E-mail: julie.trotter@anu.edu.au